A short, sharp pulse of potassium-rich volcanism during continental collision and subduction

M.R. Palmer[1], E.Y. Ersoy[2], C. Akal[2], İ. Uysal[3], Ş.C. Genç[4], L.A. Banks[1], M.J. Cooper[1], J.A. Milton[1], K.D. Zhao[5]

1. School of Ocean and Earth Science, University of Southampton, Southampton SO14 3ZH, U.K.
2. Dokuz Eylül Üniversitesi, Mühendislik Fakültesi, Jeoloji Mühendisliği Bölümü, TR-35160 İzmir, Turkey
3. Karadeniz Technical University, Dept. of Geological Engineering TR-61080 Trabzon, Turkey
4. İstanbul Technical University, Dept. of Geological Engineering, TR-34469 İstanbul, Turkey
5. State Key Laboratory of Geological Processes and Mineral Resources, Faculty of Earth Resources, China University of Geosciences, Wuhan 430074, P. R. China

ABSTRACT

Potassic volcanic rocks are characteristic of collisional tectonic zones, with recycling of continental crust playing an important role in their generation. Potassium-rich partial melts and/or fluids derived from subducted continental material initiate and/or mix with mantle-derived melts and then erupt at the surface with varying degrees of interaction with the overlying lithosphere. The details of how continental material incorporates into mantle melts are, however, uncertain. In particular, the depths from which the potassium-rich fluids/melts are released from the continental material and then reacts

with the mantle-derived melts remain a subject of debate. We have measured the boron isotope composition of volcanic rocks from Western Anatolia that erupted between 52–0.1 Ma, and span the lifetime of collisional events from initial arc-type eruptions to post-collisional volcanism. These data and other geochemical indices show that ultra-potassic volcanism was mainly confined to a narrow window between ~20–15 Ma, consistent with recycling of high-pressure phengite, with the timing of the potassic volcanism coincident with slab roll-back and break-off.

INTRODUCTION

Subduction of the lithosphere during collisional tectonics results in the production of melt in the overlying mantle that ascends to form volcanic rocks. The petrologic, elemental and isotopic composition of these rocks reflects varying admixtures of; a) recycled components from the subducted slab, b) melts of the overlying mantle and c) assimilation of upper crustal material. In particular, subduction zone volcanic rocks are commonly enriched in fluid mobile elements, such as the alkali elements and boron (Spandler and Pirard, 2013). It is noteworthy, however, that potassium-rich rocks (>3 wt.% K_2O) with high MgO concentrations >3 wt.% (e.g., lamproites and shoshonites) are largely restricted to continent-continent collision settings, where they most commonly form during the post-collisional phase of volcanism (Foley et al., 1987). Hence, continental crust recycling is commonly invoked as playing an important role in the generation of these potassic lavas (Prelević et al., 2008; Çoban et al., 2012; Ersoy and Palmer, 2013). The mechanism(s) by which potassic melts are produced is, however, subject to debate. For example, it is proposed that they are generated by; a) partial melting of sub-continental lithospheric mantle by rising asthenospheric mantle (Xu et al., 2017), b) metasomatism of harzburgite by partial melts of glimmerite (Förster et al., 2017), c) partial melting of phlogopite-harzburgite (Condamine et al., 2016), and d) partial melting of

phlogopite-free mixtures of phyllite and dunite (Wang et al., 2017). An important constraint on the mechanism operating in any particular setting is provided by the depth at which continentally-sourced K-rich melts/fluids mix with the mantle component of potassic lavas.

WESTERN ANATOLIA VOLCANIC PROVINCE

Western Anatolia (WA) forms part of the Alpine-Himalayan orogenic belt and contains a record of volcanism linked to the subduction of Tethyan oceanic crust, followed by continental collision, crustal subduction and accretion (e.g. Pourteau et al., 2016). The region has received extensive study (see Ersoy and Palmer (2013) and papers therein) and while there are subtle variations in the timing of events across the area, overall there is a progression from low-K, calc-alkaline volcanism in the Eocene and Oligocene, to a period of high-K calc-alkaline and associated shoshonitic-ultrapotassic rocks in the Miocene; ending with the eruption of Na-alkaline basalts in the Late Miocene to Holocene. This volcanic sequence reflects a progression from; arc volcanism – continental collision – post-collisional volcanism in extensional basins – final stage, OIB-like, asthenosphere-derived volcanism.

We have undertaken a boron isotope ($\delta^{11}B$) study of samples that span the full range of Eocene-Quaternary volcanism observed in WA (Fig. 1a). Together with previously published $\delta^{11}B$ (Tonarini et al., 2005) and other geochemical data (Ersoy and Palmer, 2013) from WA, we have sought to obtain a more detailed understanding of the genesis of high-K volcanic rocks in continental collision zones.

BORON ISOTOPE GEOCHEMISTRY

The $\delta^{11}B$ values and boron concentrations [B] of WA volcanic rocks range from -31.3 to +6.1 ‰ and 3.4 to 74.8 μg/g, respectively (GSA Data Repository[1]). Boron is incompatible during fractional crystallization of the volcanic rock types considered here (Leeman and Sisson,

1996), and within the calc-alkaline suite, the rocks with the highest SiO_2 and lowest MgO have the highest [B]. Overall, however, there is no significant correlation between [B] or $\delta^{11}B$ values with SiO_2 or MgO concentrations across the entire data set, or within any of the other volcanic groups (Fig. DR1, Table DR2). Similarly, no significant correlations exist between [B] or $\delta^{11}B$ values with Sr, Nd or Pb isotope ratios (Fig. DR2). Additionally, [B] and $\delta^{11}B$ values of the local continental crust, the Paleozoic-Mesozoic Menderes Massif, (4.3 to 25.8 μg/g and -14.6 to -11.0 ‰, respectively; Table DR2) do not provide appropriate end-members to describe the [B]–$\delta^{11}B$ relationships of the WA volcanic rocks by assimilation-fraction crystallization (AFC) processes (Fig. 1b).

Like potassium, boron is highly mobile during subduction and its isotope composition is a tracer of the processes and pathways of recycling and fluid transfer during collisional tectonics. All collisional zone volcanic rocks, regardless of provenance, have elevated boron concentrations [B] relative to the depleted mantle ([B] ~ 0.1 μg/g; $\delta^{11}B$ -7 ‰; Marschall et al., (2017)). Hence, the $\delta^{11}B$ values of collisional zone volcanic rocks are dominated by contributions from the slab and the upper plate through which the lavas erupted. In island arc settings, there is a general trend from heavier $\delta^{11}B$ values (up to +10 ‰) and lower Nb/B in volcanic rocks erupted close to the subduction front, towards more mantle-like $\delta^{11}B$ values and higher Nb/B at greater distances behind the subduction front and greater depths to the subducted plate (De Hoog and Savov, 2017) (Fig. 2). Continental arcs (such as the Andes) show similar trends to island arcs, but with lighter $\delta^{11}B$ values (down to -10 ‰) that reflect upper crustal assimilation. Approximately half the WA volcanic rocks fall within the range of $\delta^{11}B$ values observed in island and continental arcs, but the remainder have lighter $\delta^{11}B$ values, suggesting that they also contain boron from an ^{11}B-depleted source (Fig. 2).

TEMPORAL EVOLUTION

The temporal evolution of boron isotopes and other geochemical signatures yields insights into the origin of the high-K WA volcanic rocks. Overall, the period from the Lower Eocene to the present can be divided into three overlapping phases (Fig. 3). From the Lower Eocene to Lower Miocene (~52 to 23 Ma), the $\delta^{11}B$ systematics are typical of those seen in the arc settings (De Hoog and Savov, 2017) (Fig. 3a-b). There then follows a period of more heterogeneous (post-orogenic/collisional) volcanism during the Lower to Upper Miocene (~23 to 14 Ma) that contains rocks with arc-type signatures, but this also marks the period when the ultra-potassic rocks with the highest [B] and most negative $\delta^{11}B$ values were erupted. The final period of volcanism, from the Upper Miocene to Recent (~12 to 0.1 Ma), marks the eruption of rocks with more mantle-like signatures (Fig. 3a-c).

We suggest here, that incorporation of boron derived from phengite is the likely source of the negative $\delta^{11}B$ values. Phengite, with $\delta^{11}B$ values of -29 ‰, is recorded in exhumed ultra-high pressure (UHP) rocks from the Luliang Shan terrane in NW China (Menold et al., 2016), where it is suggested that it formed in continental crust subducted to depths of ~75 km. These light values likely arise because ^{11}B is progressively fractionated into the fluid phase during devolatilization as the slab is subducted into the mantle (Marschall et al., 2007), leaving the residual phengite with increasingly light $\delta^{11}B$ values. Although this process also results in progressive depletion of boron in the slab, [B] of up to 250 μg/g is recorded in UHP phengite (Menold et al., 2016). Thus, incorporation of boron derived from recycling of deeply subducted phengite may account for the light $\delta^{11}B$ values observed in some WA volcanic rocks. Phengite pressure depends strongly on the water activity, but in sediment-rich systems it typically breaks down at 2.5-5.0 GPa to form a K-rich melt that rises into the overlying mantle wedge to form phlogopite or K-richterite (Schmidt and Poli, 2014). These melts are then suggested to lead to the formation of ultrapotassic volcanic rocks in collisional settings (Zheng et al., 2011).

125 The $\delta^{11}B$ values and [B] in exhumed phengite from the Luliang Shan terrane range from
126 -29 to -7 ‰ and 50 to 250 μg/g, respectively (Menold et al,. 2016). This range and absence of
127 a clear correlation between [B] and $\delta^{11}B$ values likely reflects the geochemical and
128 mineralogical heterogeneity (in space and time) of subducted continental crust, particularly for
129 trace elements such as boron. When this observation is coupled with the evolving P-T
130 conditions and fluid-flow regimes during subduction, a direct correlation between $\delta^{11}B$ values
131 and potassium enrichment in individual volcanic rocks is not necessarily expected.
132 Nevertheless, formation of phengite with light $\delta^{11}B$ values is likely a common feature in
133 continental material subducted to UHP conditions (Konrad-Schmolke and Halama, 2014;
134 Menold et al,. 2016), and the coincidence between the timing of the light $\delta^{11}B$ values measured
135 in the WA volcanic rocks with the period of potassic volcanism is supportive of recycling
136 deeply subducted continental crust.

137 Further support for this hypothesis comes from the evolution of the K_2O/Na_2O ratio of
138 WA volcanic rocks, which show a discrete interval of high K_2O/Na_2O ratios (from ~2 to 6)
139 erupted between ~20–15 Ma (Fig. 3d). This observation is important because the K_2O/Na_2O
140 ratio produced during partial melting of pelitic rocks is dependent on pressure (Schmidt, 2015),
141 with a 10% metapelite partial melt yielding a K_2O/Na_2O ratio of 5 at 5 GPa, compared to a
142 K_2O/Na_2O ratio of 1.5 at 3 GPa. The K_2O/Na_2O ratio is also dependent on the water content of
143 the metapelite, with experiments conducted with 7 wt. % H_2O yielding a K_2O/Na_2O ratio of
144 <1.75 at 5 GPa compared to a ratio >5 at the same pressure with 2 wt. % H_2O (Schmidt, 2015).
145 Comparison of the WA data and experimental studies suggests, therefore, that high K_2O/Na_2O
146 ratio melts were generated at pressures of >3 GPa. Evidence that the K-rich rocks were derived
147 from deep mantle processes also comes from the evolution of Tb/Yb and Ti/Yb ratios in the
148 WA volcanic rocks (Fig. 3e-f). Both ratios increase in ultrapotassic rocks erupted between 20-

15 Ma, and are consistent with an increased presence of garnet in the source – i.e. an increase in the depth of mantle melting (Ersoy and Palmer, 2013).

Overall, the strongly negative $\delta^{11}B$ values are most compatible with breakdown/partial melting of phengite subducted to pressures of >3 GPa to produce phlogopite/K-richterite in the overlying mantle. This hypothesis precludes a model of partial melting of phlogopite-free mixtures of phyllite and dunite (Wang et al., 2017), and the absence of negative $\delta^{11}B$ values and high K_2O/Na_2O ratios in the OIB-type volcanics (Fig. 3) suggests that asthenospheric melts did not play a direct role in generation of the WA ultrapotassic volcanism (cf. Xu et al., 2017). Both the phlogopite-harzburgite and glimmerite-harzburgite experimental studies yield melts with K_2O/Na_2O ratios similar to those observed in the WA ultrapotassic rocks (Condamine et al., 2016; Förster et al., 2017). Hence, the $\delta^{11}B$ – K_2O/Na_2O data support a model whereby continental material is subducted to depths of >75 km at which point phengite with strongly negative $\delta^{11}B$ breaks down to yield potassic melts that initiate melting of the overlying lithospheric mantle to produce the ultrapotassic volcanism.

Mantle tomographic images of Western Anatolia have been interpreted to indicate that there was a “dramatic increase” in slab roll-back triggered by slab tearing in WA at ~15 Ma (van Hinsbergen et al., 2010) – i.e. coincident with eruption of the high K_2O/Na_2O ratio volcanic rocks. This event may thus have accelerated descent of the subducted continental material into a P-T regime that initiated phengite breakdown and contamination of the overlying mantle. Partial melting of the contaminated mantle then led to a brief period (~5 Myr) of high-potassium volcanism, with the variable $\delta^{11}B$ and K_2O/Na_2O ratios reflecting the heterogeneous nature of subducted continental material (Soder and Romer, 2018). The increased slab roll-back led to inflow of uncontaminated asthenospheric mantle, which abruptly terminated the high-potassium volcanism and initiated OIB-like Na-alkaline volcanism.

Advances in seismic tomography have allowed for the identification of detached slabs throughout the mantle and for the correlation of mantle slabs to specific orogens (van der Meer et al., 2018). The timing of slab detachment is generally based on dating metamorphic and volcanic processes within an orogeny that may take place over a period of ~100 Myr. The age range of slab detachment and can then be used to provide upper and lower bounds for the rate of slab sinking and mantle viscosity. If, as we hypothesize, high-potassium volcanism is directly linked to slab roll-back and detachment it may be possible to provide a specific date for initiation of this process, thereby providing closer constraints on fundamental processes operating in the upper mantle.

ACKNOWLEDGEMENTS

This research was funded by TUBITAK grant #112Y128. We are grateful to Horst Marschall and two anonymous reviewers for their helpful comments.

REFERENCES CITED

Çoban, H., Karacık, Z., and Ece, Ö.I., 2012, Source contamination and tectonomagmatic signals of overlapping Early to Middle Miocene orogenic magmas associated with shallow continental subduction and asthenospheric mantle flows in Western Anatolia: A record from Simav (Kütahya) region. Lithos, v. 140-141, p. 119-141, doi.org/10.1016/j.lithos.2011.12.006.

Condamine, P., Médard, E., and Devidal, J.L., 2016, Experimental melting of phlogopite-peridoite in the garnet stability field: Contributions to Mineralogy and Petrology, v. 171, 95, doi:10.1007/s00410-016-13-6-0.

196 De Hoog, J.C.M., and Savov, I.P., 2017, Boron isotopes as a tracer of subduction zone
197 processes, *in* Marschall, H.R., and Foster, G.L., eds., Boron Isotopes: The Fifth
198 Element. Springer Nature, Switzerland, 289 pp, doi:10.1007/978-3-319-64666-4.
199 Ersoy, E.Y., and Palmer, M.R., 2013. Eocene-Quaternary magmatic activity in the Aegean:
200 implications for mantle metasomatism and magma genesis in an evolving orogeny:
201 Lithos 180–181, 5-24, doi:10.1016/j.lithos.2013.06.007
202 Foley, S.F., Venturelli, G., Green, D.H., and Toscani, L., 1987, The ultrapotassic rocks:
203 Characteristics, classification, and constraints for petrogenetic models: Earth-Science
204 Reviews, v. 24, p. 81-134, doi:10.1016 /0012-8252 (87)90001-8.
205 Förster, M.W., Prelević, D., Schmück, H.R., Buhre, S., Veter, M., Mertz-Kraus, R., Foley, S.F.,
206 and Jacob, D.E., 2017, Melting and dynamic metasomatism of mixed
207 harzburgite+glimmerite mantle source: Implications for the genesis of orogenic
208 potassic magmas: Chemical Geology, v. 455, p. 182-191, doi: 10.1016/
209 j.chemgeo.2016.08.037.
210 Konrad-Schmolke, M., and Halama, R., 2014, Combined thermodynamic-geochemical
211 modeling in metamorphic geology: Boron as a tracer of fluid-rock interaction: Lithos,
212 v. 208-209, p. 393-414, doi:10.1016/j.lithos.2014.09.021.
213 Leeman, W.P., and Sisson, V.B., 1996, Geochemistry of boron and its implications for crustal
214 and mantle processes: Reviews in Mineralogy, v. 33, p. 645-708.
215 Marschall, H.R., Altherr, R., and Rüpke, L., 2007, Squeezing out the slab – Modelling the
216 release of Li, Be and B during progressive high-pressure metamorphism: Chemical
217 Geology, v. 239, p. 323-335, doi:10.1016/j.chemgeo.2006.08.008.
218 Marschall, H.R., Wanless, V.D., Shimizu, N., Pogge von Strandmann, P.A.E., Elliott, T., and
219 Monteleone, B.D., 2017, The boron and lithium isotope composition of mid-ocean

ridge basalts and the mantle: Geochimica et Cosmochimica Acta, v. 207, p. 102-138, doi:10.1016/j.gca.2017.03.028.

Menold, C.A., Grove, M., Sievers, N.E., Manning, C.E., Yin, A., Young, E.D., and Ziegler, K., 2016, Argon, oxygen, and boron isotopic evidence documenting 40ArE accumulation in phengite during water-rich high-pressure subduction metasomatism of continental crust: Earth and Planetary Science Letters, v. 446, p. 56-67, doi: 10.1016/j.epsl.2016.04.010.

Pourteau, A., Oberhänsli, R., Candan, O., Barrier, E., and Vrielynck, B., 2016, Neothethyan closure history of western Anatolia: a geodynamic discussion: International Journal of Earth Science, v. 105, p. 203-224, doi: 10.1007/s00531-015-1226-7.

Prelević, D., Foley, S.F., Romer, R., and Conticelli, S., 2008, Mediterranean Tertiary lamproites derived from multiple source components in postcollisional geodynamics: Geochimica et Cosmochimica Acta, v. 72, p. 2125-2156, doi:10.1016 /j.gca.2008.01.029.

Schmidt, M.W., and Poli, S., 2014, Devolatilization during subduction: *in* Holland H.D., and Turekian, K.K., eds. Treatise on Geochemistry 2nd ed., v. 3, p. 669-700, doi:10.1016/B978-0-08-095975-7.00321-1.

Schmidt, M.W., 2015, Melting of pelitic sediments at subarc depths: Melt chemistry, viscosities and a parameterization of melt composition: Chemical Geology, v. 404, p. 168-182, doi:10.1016/j.chemgeo.2015.02.013.

Soder, C., and Romer, R.L., 2018, Post-collisional potassic-ultrapotassic magmatism of the Variscan Orogen: implications for mantle metasomatism during continental subduction: Journal of Petrology, in press, doi:10.1093/petrology/egy053.

Spandler, C., and Pirard, C., 2013, Element recycling from subducting slabs to arc crust: A review: Lithos, v. 170-171, p. 208–223, doi:10.1016 /j .lithos.2013.02.016.

Tonarini, S., Agostini, S., Innocenti, F., and Manetti, P., 2005, $\delta^{11}B$ as tracer of slab dehydration and mantle evolution in Western Anatolia Cenozoic magmatism: Terra Nova, v. 17, p. 259-264, doi:10.1111/j.1365-3121.2005.00610.x.

Wang, Y., Foley, S.F., and Prelević, D., 2017 Potassium-rich magmatism from a phlogopite-free source: Geology, v. 45, p. 467-470, doi:10.1130/G38691.1.

van der Meer, D.G., van Hinsbergen, D.J.J., and Spakman, W., 2018, Atlas of the underworld: Slab remnants in the mantle, their sinking history and a new outlook on lower mantle viscosity: Tectonophysics, v. 23, p. 309-448, doi: 10.1016/j.tecto.2017.10.004.

van Hinsbergen, D.J.J., Kaymakci, N., Spakman, W., and Torvik, T.H., 2010, Reconciling the geological history of western Turkey with plate circuits and mantle tomography: Earth and Planetary Science Letters, v. 297, p. 674-686, doi: 10.1016/j.epsl.2010.07.024.

Xu, B., Griffin, W.L., Xiong, Q., Hou, Z.Q., O'Reilly, S., Guo, Z., Pearson, N.J., Gréau, Y., Yang, Z.M., and Zheng, Y.C., 2017, Ultrapotassic rocks and xenoliths from South Tibet: Contrasting styles of interaction between lithospheric mantle and asthenosphere during continental collision: Geology, v. 45, p. 51-54, doi:10.1130/G38466.1.

Zheng, Y.F., Xia, Q.X., Chen, R.X., and Gao, X.Y., 2011, Partial melting, fluid supercriticality and element mobility in ultrahigh-pressure metamorphic rocks during continental collision: Earth Science Reviews, v. 107, p. 342-374, doi: 10.1016/j.earscirev.2011.04.004.

FIGURE CAPTIONS

Figure 1.

(a) K_2O wt.% vs SiO_2 wt.%. Samples analysed for $\delta^{11}B$ shown in bold, with other data from Ersoy and Palmer (2013) and references therein.

(b) $\delta^{11}B$ ‰ vs B μg/g. Colours of symbols reflect classification in Figure 1a. Stars are from Menderes Massif. Data from this study and Tonarini et al. (2005).

Figure 2. Nb/B vs $\delta^{11}B$ ‰. Symbols as in Figure 1. Arc data from De Hoog and Samov (2017) and references therein. WA data from Ersoy and Palmer (2013) and references therein.

Figure 3. Geochemical evolution of Western Anatolian volcanic rocks. Samples analysed for $\delta^{11}B$ shown in bold, with other data from Ersoy and Palmer (2013) and references therein.

(a) $\delta^{11}B$, (b) [B], (c) K_2O, (d) K_2O/Na_2O, (e) Tb/Yb, (f) Ti/Yb

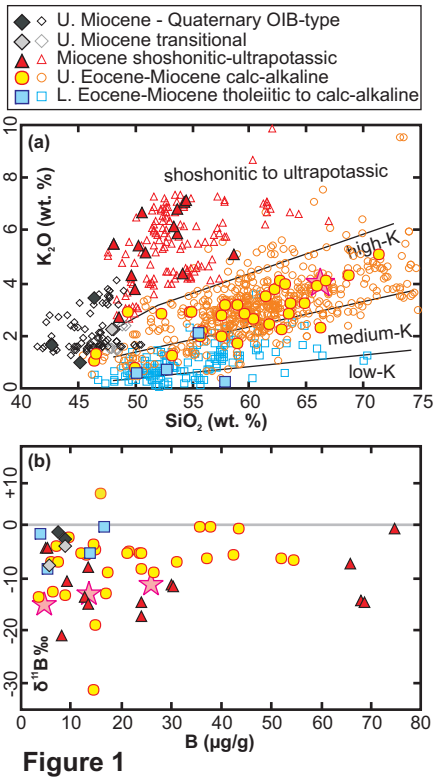
U. Miocene - Quaternary OIB-type
U. Miocene transitional
Miocene shoshonitic-ultrapotassic
U. Eocene-Miocene calc-alkaline
L. Eocene-Miocene tholeiitic to calc-alkaline
(a)
shoshonitic to ultrapotassic
high-K
medium-K
low-K
K2O (wt. %)
SiO2 (wt. %)
(b)
δ11B‰
B (µg/g)

Figure 1

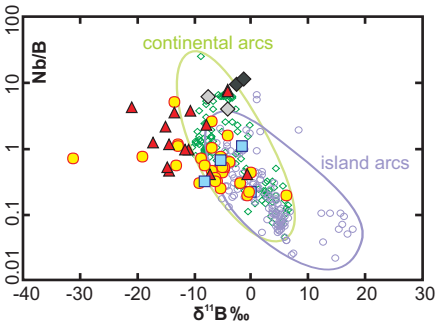
continental arcs
island arcs
Nb/B
100
10
1
0.1
0.01
-40
-30
-20
-10
0
10
20
30
δ11B ‰

Figure 2

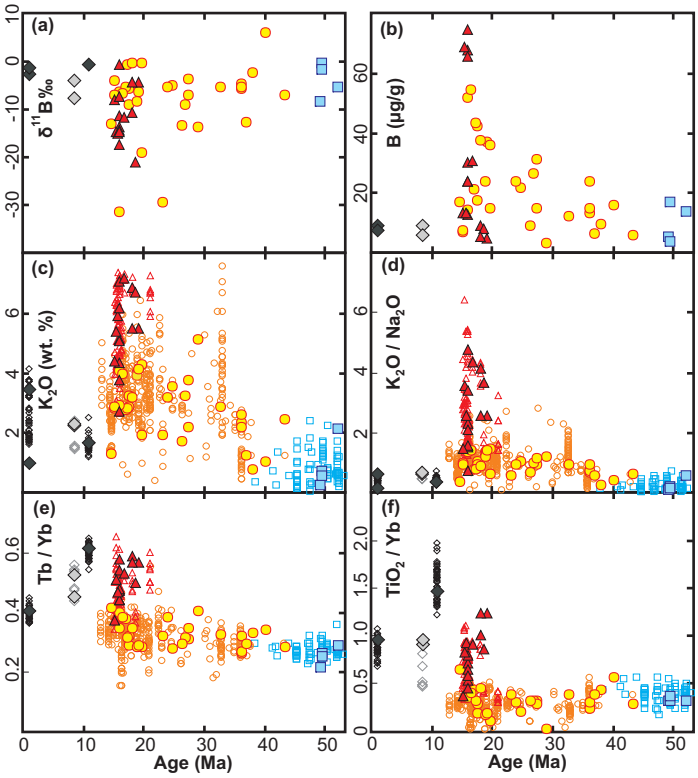

Figure 3

A short, sharp pulse of potassium-rich volcanism during continental collision and subduction

SUPPLEMENTARY FILE

ANALYTICAL METHODS

The analytical method for determining the boron concentration and isotope composition of the samples has been adapted from Wei et al. (2013). All the reagents used were high purity and all the sample processing took place in clean laboratories equipped with boron-free HEPA filters at the University of Southampton.

Approximately 100 mg of rock powder was accurately weighed and transferred into a 7 ml screw top PFA vial, together with 100 μL of 1% mannitol, 100 μL H_2O_2 and 1 mL 24 M HF. The vial was sealed and placed on a hot plate for 3 days at 60^{o}C. A white precipitate, consisting largely of fluorite, was present in the sample solution after this time. Dissolution of this precipitate and analysis by inductively coupled plasma mass spectrometry (ICP-MS) revealed that it did not contain any detectable boron, in accordance with previous observations (Nakamura et al., 1992; Wei et al., 2013). After dissolution, 0.5 mL of the sample was added to 1.5 mL of water in a polypropylene centrifuge tube. After centrifuging, the supernatant was transferred to another 7 mL PFA vial and a further 2 mL of water was added to yield a 3 M HF solution.

The boron concentration was determined by taking 0.1 mL of the 3 M HF sample solution and diluting to 5 mL with 3% HNO_3 containing a 10 ng/g Be internal standard. The boron concentration was then determined using a Thermo Element high-resolution (HR) ICP-MS against a range of 0 to 5 ng/g boron standards (also containing 10 ng/g Be).

Boron was separated from the solution using Bio-Rad AG MP-1 anion exchange resin. The columns consisted of a polypropylene funnel fitted with a porous frit. A fresh aliquot of ~100 μL of resin was loaded into the stem of the funnel for each separation. The overall ion

exchange chromatography procedure is summarized in Table DR1. The sample load volume was adjusted so that ~100 ng of boron was added to the column. The boron fraction was collected in a 7 mL PFA vial to which 10 μL of 1% mannitol was added and the solution was evaporated to dryness at 55°C.

The sample was taken up in 0.5 mL of 0.5 M HNO_3 to yield a solution with ~200 ng/g boron. Boron isotope analyses were then carried out using a Thermo Neptune multi-collector (MC) ICP-MS following the method described in Foster (2008) that was modified with the use of a 0.3 M HF/0.5 M HNO_3 wash solution to speed up the wash-out time. The NIST SRM 951 boric acid standard (200 ng/g) was used during the sample-standard bracketing and to define the $\delta^{11}B$ values of the samples. Typical in-run 2σ precisions were <0.2 ‰.

During this study, all samples were analyzed in batches of 10. Each batch consisted of duplicates of 4 powdered rock samples, a powdered rock reference material and a blank. Thus each sample was independently analyzed for both its concentration and $\delta^{11}B$ value at least twice, and 7 samples were analyzed in triplicate. The blank after sample dissolution was always <0.5 ng and typically <0.1 ng. The blank associated with the ion exchange chromatography was always <1 ng of boron and typically <0.3 ng (compared to a sample analyte of ~100 ng of boron). The largest difference between the highest and lowest $\delta^{11}B$ replicate analyses of a sample was 1.0 ‰, with the average difference being 0.3 ‰ (Table DR2). The largest difference between the highest and lowest boron concentration [B] replicate analyses of a sample was 10.7 % of the absolute value, with the average difference being 3.7 %. During this study, 10 analyses of standard IAEA-B5 (basalt from Etna volcano; Gonfiantini et al., 2003) yielded an average $\delta^{11}B$ value of -4.2 ± 0.2 ‰ (2σ) and an average [B] of 9.2 ± 0.2 μg/g (2σ). These values compare well with values previously obtained for this reference material (Table DR3).

In addition to the 42 $\delta^{11}B$ and [B] data listed in Table 2, Tonarini et al. (2005) report data for 16 WA volcanic rocks. They did not analyse the IAEA-B5 reference material, but they report a $\delta^{11}B$ value of 7.3 ± 0.4 ‰ for the GSJ-JB2 basalt reference material. Four analyses of this reference material in this study yielded average $\delta^{11}B$ and [B] values of 7.2 ± 0.2 ‰ and 29.4 ± 0.7 μg/g, respectively. Hence, the $\delta^{11}B$ values within the two data sets are directly comparable.

ADDITIONAL REFERENCES CITED

Berryman, E.J., Kutzschbach, M., Trumbull, R.B., Meixner, A., van Hinsberg, V., Kasemann, S.A., and Franz, G., 2017, Tourmaline as a petrogenetic indicator in the Pfitsch Formation, Western Tauern Window, Eastern Alps: Lithos, v. 284-285, p. 138-155, doi: 10.1016/j.lithos.2017.04.008.

Foster, G.L., 2008, Seawater pH, pCO_2 and [CO_3^{2-}] variations in the Caribbean Sea over the last 130 kyr: A boron isotope and B/Ca study of planktic foraminifera: Earth and Planetary Science Letters, v. 271, p. 254-266, doi:10.1016/j.epsl.2008.04.015.

Gonfiantini, R., and 30 others, 2003, Intercomparison of boron isotope and concentration measurements. Part II: Evaluation of results: Geostandards Newsletter, v. 27, p. 41-57, doi:10.1111/j.1751-908X.2003.tb00711.x.

Hansen, C.T., Meixner, A., Kasdemann, S.A., and Bach, W., 2017, New insight on Li and B isotope fractionation derived from batch reaction investigations: Geochimica et Cosmochimica Acta, v. 217, p. 51-79, doi: 10.1016/j.gca.2017.08.014 0016-7037/2017.

Nakamura, E., Ishikawa, T., Birck, J.L., and Allegre, C.J., 1992, Precise boron isotopic analysis of natural rock samples using a boron-mannitol complex: Chemical Geology, v. 94, p. 193-204, doi:10.1016/0168-9622(92)90012-Y.

Pi, J.L., You, C.F., Chung, C.H., Micro-sublimation separation of boron in rock samples for isotopic measurement by MC-ICP-MS. Journal of Analytical Atomic Spectrometry, 29, 861-867, DOI: 10.1039/c3ja50344e

Romer, R.L., Meixner, A., and Hahne, K., 2014, Lithium and boron isotopic composition of sedimentary rocks- The role of source history and depositional environment: A 250 Ma record from the Cadomian orogeny to the Variscan orogeny: Gondwana Research, v. 26, p. 1093-1110, doi: 10.1016/j.gr.2013.08.015.

Wei, G., Wei, J., Liu, Y., Ke, T., Ren, Z., Ma, J., and Xu, Y., 2013, Measurement on high-precision boron isotope of silicate materials by a single column purification method and MC-ICP-MS: Journal of Analytical Atomic Spectrometry, v. 28, p. 606-612, doi: 10.1039/C3JA30333K.

FIGURE CAPTIONS

Figure DR1.

Harker diagrams for WA volcanic rocks

(a) [B] μg/g vs. SiO_2 wt%, (b) [B] μg/g vs. MgO wt%, (c) $\delta^{11}B$ ‰ vs. SiO_2 wt%, (d) $\delta^{11}B$ vs. MgO wt%. Major element data from Ersoy and Palmer (2013), and references therein.

Figure DR2.

[B] and $\delta^{11}B$ values versus radiogenic isotope ratios

(a) [B] μg/g vs $^{87}Sr/^{86}Sr$, (b) $\delta^{11}B$ ‰ vs $^{87}Sr/^{86}Sr$, (c) $\delta^{11}B$ ‰ vs $^{143}Nd/^{144}Nd$, (d) $\delta^{11}B$ ‰ vs $^{208}Pb/^{204}Pb$. Radiogenic isotope data from Ersoy and Palmer (2013), and references therein.

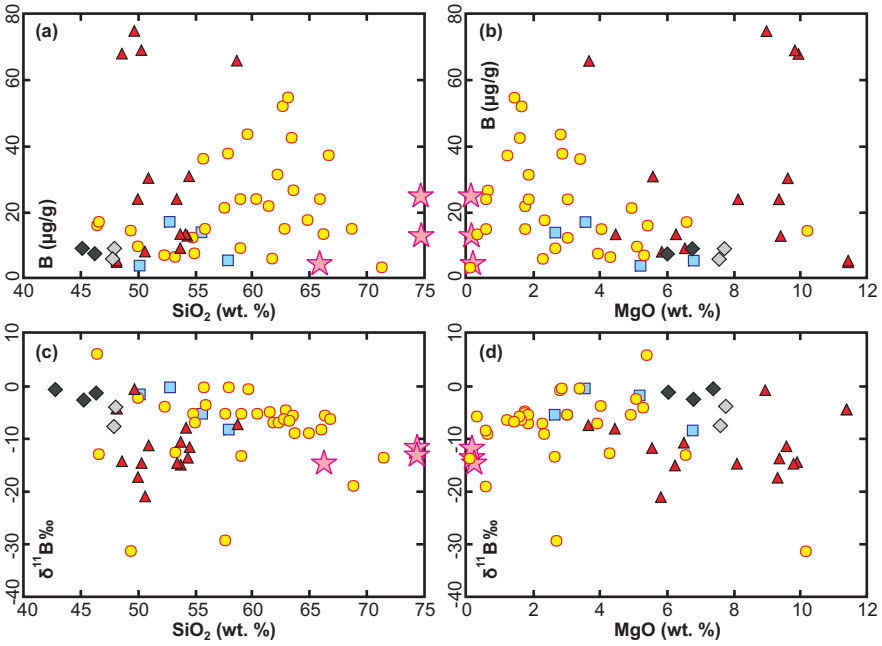

Figure DR1

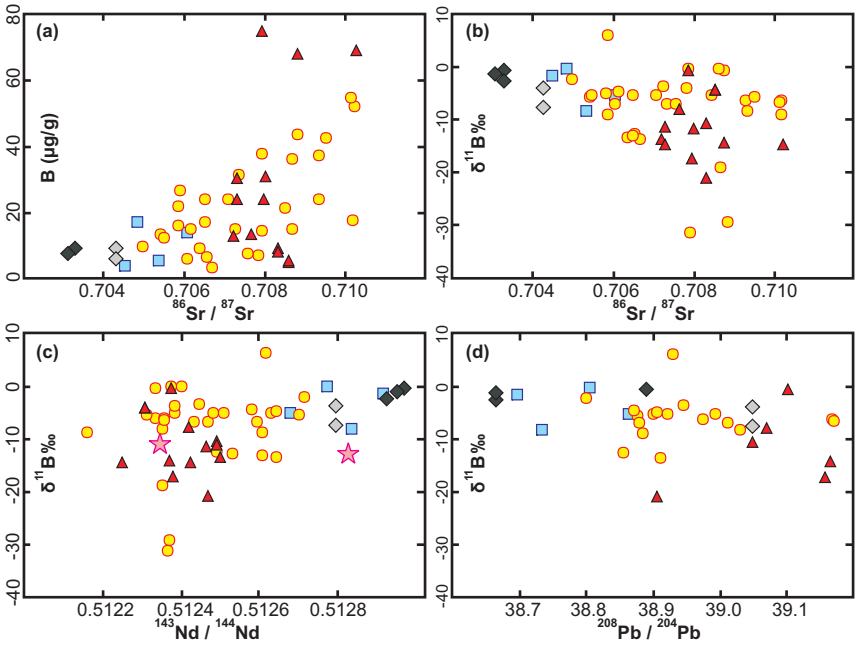
(a)
B (µg/g)
0
20
40
60
80
0.704
0.706
0.708
0.710
86Sr / 87Sr
(b)
δ11B ‰
10
0
-10
-20
-30
-40
0.704
0.706
0.708
0.710
86Sr / 87Sr
(c)
δ11B‰
10
0
-10
-20
-30
-40
0.5122
0.5124
0.5126
0.5128
143Nd / 144Nd
(d)
δ11B‰
10
0
-10
-20
-30
-40
38.7
38.8
38.9
39.0
39.1
208Pb / 204Pb

Figure DR2

Table DR1
Ion exchange chromatography procedure

Step	Operation
Step 1	Resin washing and conditioning
	2.5 mL H_2O
	0.5 mL 24 M HF
	1.5 mL H_2O
Step 2	Sample loading
	3 M HF (volume adjusted according to sample)
Step 3	Matrix elution
	2 x 0.5 mL H_2O
	8.5 mL 0.1 M HCl
Step 4	Boron collection
	1.2 mL 24 N HF

Table DR2.
Boron concentration and isotope data for samples analysed in this study (UTM coordinates give sample location)

	B concentration (μg/g)				**δ^{11}B (‰)**			
Sample (UTM)	**1st run**	**2nd run**	**3rd run**	**mean**	**1st run**	**2nd run**	**3rd run**	**mean**
Early Eocene orogenic (Kizderbent volcanics)								
G5 (0651592/4488750)	5.2	5.1		**5.2**	-8.3	-8.3		**-8.3**
G28 (0651592/4488750)	16.9	16.8	16.6	**16.8**	-0.6	-0.5	0.2	**-0.3**
G45 (0749558/4499472)	3.8	3.7		**3.8**	-1.7	-1.6		**-1.6**
G48 (0737486/4502470)	14.2	13.6	13.9	**13.9**	-5.2	-5.3	-5.7	**-5.4**
Middle Eocene – Miocene orogenic (Late Eocene Balıklıçeşme volcanics)								
B5 (0492827/4448313)	16.1	16.3	16.0	**16.1**	6.3	6.2	5.8	**6.1**
B11 (0500469/4459685)	12.9	13.3		**13.1**	-5.5	-5.8		**-5.7**
B12 (0486130/4466913)	14.6	14.9		**14.7**	-4.6	-4.7		**-4.7**
B17 (0473433/4454350)	23.1	24.0	23.7	**23.6**	-5.7	-5.3	-4.8	**-5.3**
B35 (0485295/4455090)	9.9	9.3		**9.6**	-2.2	-2.2		**-2.2**
C15 (0481003/4413380)	6.4	6.0		**6.2**	-12.6	-13.1		**-12.8**
C42 (0466010/4432014)	6.2	5.6		**5.9**	-7.0	-7.3		**-7.1**
(Oligocene Kirazlı volcanics)								
B21 (0477628/4444050)	3.4	3.4		**3.4**	-13.7	-13.5		**-13.6**
C7 (0480017/4430858)	11.9	12.0		**12.0**	-5.2	-5.2		**-5.2**
C9 (0477916/4420541)	14.6	14.4	14.7	**14.6**	-3.8	-3.7	-4.1	**-3.8**
C31 (0497168/4425055)	26.5	26.7		**26.6**	-8.9	-9.4		**-9.1**
C36 (0474152/4433482)	21.0	21.9		**21.5**	-5.1	-4.8		**-5.0**
(Oligocene Hallaçlar volcanics)								
HG2 (0530735/4407610)	31.0	31.1		**31.1**	-6.8	-7.0		**-6.9**
HG9 (0536865/4436733)	24.0	24.3	23.9	**24.1**	-5.0	-5.4	-5.1	**-5.2**
(Oligocene Keşan volcanics)								
K20 (0469494/4521168)	8.5	9.4		**9.0**	-13.2	-13.2		**-13.2**
(Miocene Yuntdağı volcanics)								

129 (0540981/4353496)	15	14.3		**14.7**	-19.1	-19.1	5.8	**-19.1**
(Miocene Yağcıdağ volcanics)								
510 (0657381/4302983)	49.7	54.6		**52.1**	-6.1	-6.3		**-6.2**
YF2 (0657381/4302983)	53.5	55.4	54.1	**54.3**	-6.6	-6.5	-6.3	**-6.5**
(Miocene Eğreltidağ volcanics)								
521 (0657795/4308366)	25.1	23.1		**24.1**	-8.6	-8.1		**-8.4**
(Miocene Sevinçler volcanics)								
718 (0652561/4322172)	36.7	37.4		**37.1**	-6.4	-6.4		**-6.4**
(Miocene Miocene Asitepe volcanics)								
754 (0636380/4309275)	42.8	42.1		**42.5**	-5.7	-5.3		**-5.5**
(Miocene Yaylaköy volcanics)								
L36 (0453515/4270500)	21.7	20.5		**21.1**	-5.6	-5.8		**-5.4**
(Miocene Armağandağ volcanics)								
L47 (0451794/4236840)	43.7	43.2		**43.5**	-0.8	-0.8		**-0.8**
(Miocene Kuzayır lamproite)								
518 (0660886/4311660)	9.1	9.3		**9.2**	-11.2	-10.2		**-10.7**
528 (0660886/4311660)	8.2	7.8		**8.0**	-20.8	-21.2		**-21.0**
(Miocene Doğanca lamproite)								
K17 (0475167/4528879)	4.8	5.1		**5.0**	-4.0	-4.4		**-4.2**
K17B (0475167/4528879)	4.9	5.4		**5.2**	-4.3	-4.1		**-4.2**
(Miocene Kayacık volcanics)								
756 (0601705/4305141)	16.7	18.0		**17.4**	-9.1	-8.8		**-8.9**
(Miocene Güre lamproite)								
822 (0679728/4281490)	66.2	71.2		**68.7**	-14.7	-14.8		**-14.7**
(Miocene Karaburun volcanics)								
L30 (0458200/4275780)	14.1	14.7		**14.4**	-31.4	-31.3		**-31.3**
(Miocene Orhanlar basalt)								
536 (0680006/4311835)	24.5	23.7		**24.1**	-17.2	-17.4		**-17.3**
541 (0679810/4310909)	67.3	68.5		**67.9**	-14.7	-14.2		**-14.4**
543 (0679836/4310901)	72.8	76.7		**74.8**	-0.5	-1.0		**-0.8**
(Miocene Naşa basalt)								

746 (0671372/4333717)	13.4	13.6	**13.5**	-8.0	-8.2		**-8.1**
Transitional – Miocene (Late Miocene Kabaklar basalt)							
520-1 (0671542/4298101)	5.9	5.7	**5.8**	-7.4	-7.6	-4.8	**-7.5**
Basement Rocks (Menderes Massif - gneiss)							
G01 (0673572/4300943)	13.4	13.1	**13.3**	-13.3	-12.9		**-13.1**
G02 (0673572/4300943)	24.9	26.7	**25.8**	-11.3	-10.8		**-11.0**
(Menderes Massif - Rahmanlar granite)							
Y23-2 (0674406/4302063)	4.1	4.4	**4.3**	-14.1	-15.1		**-14.6**

Table DR3.
Boron concentration and isotope data for IAEA-B5 reference material

Source	[B] (μg/g) ± 2σ	$\delta^{11}B$ (‰)± 2σ
This study	9.2 ± 0.2	-4.2 ± 0.2
Gonfiantini et al., 2003	10.0 ± 1.2	-4.1 ± 2.7
Pi et al., 2014	9.3 ± 0.1	-3.9 ± 0.2
Romer et al., 2014	10.0 ± 1.0	-3.7 ± 0.7
Hansen et al., 2017		-4.3 ± 0.2
Berryman et al., 2017	9.3 ± 0.4	-4.3 ± 0.2